J. Fluid Mech. (2005), *vol.* 534, *pp.* 237–261.
doi:10.1017/S0022112005004155 Printed in the United Kingdom

The flow field around a rotor in axial descent

By RICHARD B. GREEN[1], ERIC A. GILLIES[1] AND RICHARD E. BROWN[2]

[1]Department of Aerospace Engineering, University of Glasgow, G12 8QQ, UK
[2]Department of Aeronautics, Imperial College, London, SW7 2AZ, UK

(Received 25 May 2004 and in revised form 12 January 2005)

Measurements of the flow field around a model rotor descending axially into its own vortex wake have been performed using particle image velocimetry (PIV). At low descent rates, the expected cylindrical down-flow structure below the rotor is observed. At slightly higher descent rate, the flow enters the so-called vortex ring state (VRS) where the vorticity from the rotor accumulates into a toroidal structure near the rotor tips, and a large recirculation zone forms above the rotor disk. In the VRS, the flow below the rotor shows a significant upwards component, with a small up-flow zone penetrating right up to the rotor disk. Measurements show there to be a range of descent rates just before the onset of the VRS over which the flow may be interpreted to be in an incipient VRS condition. In this range, analyses of individual PIV measurements indicate that the flow near the rotor intermittently switches between the down-flow topology found at lower descent rates and the flow topology found in the fully developed VRS. The frequency of excursions of the flow into the VRS topology increases as the descent rate of the rotor is increased until, at high enough descent rate, the flow remains locked within its toroidal state.

1. Introduction

The fluid mechanics of a rotor thrusting against a free-stream flow are particularly rich. Such a system has considerable practical importance as it is analogous to a helicopter rotor in axial descending flight. In particular, the flow around a descending rotor may exhibit a qualitative change in topology, in what is called the vortex ring state (VRS), where the rotor descends into its own wake. In the VRS, the helical vortex system that is usually generated by the rotor collapses to form a highly unsteady toroidal vortex system near to the rotor disk. The intermittent ejection of clumps of vorticity into the flow downstream of the rotor leads to a situation bearing some resemblance to the flow behind a three-dimensional bluff body. Entry into the VRS is potentially dangerous for helicopters, since the onset of the VRS is usually accompanied by loss of altitude, changes in control effectiveness and low-frequency pitch and roll oscillations. For rotorcraft with multiple lifting rotors, the consequences of entry into the VRS may be even more severe, especially since entry of just one rotor into the VRS may cause very large, and potentially uncontrollable, moments on the airframe. The existence of the VRS has been known since the inception of rotary-winged flight, but, since the VRS impacts a relatively small proportion of the flight envelope of traditional helicopters, it has received relatively little attention until recently. Renewed interest in the VRS has come about following a shift in design philosophy towards helicopters and tilt-rotors with more highly loaded blades, where

the VRS affects a much larger proportion of the flight envelope (notwithstanding the fact that VRS onset is postponed to higher descent rates) (Newman *et al.* 2003).

Early investigations of the VRS were largely experimental. Wind-tunnel tests on model rotors were conducted by Drees & Hendal (1951), while Stewart (1951) reported results from in-flight experiments with a variety of helicopters. It is only recently that the pioneering smoke-flow visualizations of the VRS by Drees & Hendal (1951), showing the development of the toroidal flow near the rotor, have been supplemented by other flow-visualization data. It is now widely accepted that the unsteadiness of the flow field of the rotor is a key feature of the VRS, and Stack, Caradonna & Savaş (2004), by visualizing the flow using air bubbles in water, were able to correlate the flow patterns above and below the rotor with simultaneous measurements of the thrust generated by the system. Newman *et al.* (2003) showed a limited set of flow-field data from particle image velocimetry (PIV) tests of a rotor in simulated descent. Their results show a highly unsteady flow field below the rotor, but do not show a great deal of the flow field above the rotor. Brinson & Ellenrieder (1998) conducted a limited smoke-flow visualization of the VRS, and identified a conical region of reverse flow, passing up through the rotor in the region of the hub, in addition to the toroidal vortex structure that is usually observed further outboard on the rotor disk. Further flow-visualization data (Leishman 2000), using high-resolution shadowgraph photography of a model rotor in descending flight, shows clearly the accumulation of vorticity close to the edge of the rotor disk when in the VRS. Other experimental investigations of the VRS have examined the performance of the rotor. Yaggy & Mort (1963) and Washizu *et al.* (1966) correlated the amplitude of observed thrust and power fluctuations with the descent rate of isolated model rotors, emphasizing the unsteadiness of the rotor loading in the VRS. Similar studies were conducted by Betzina (2001) for a tilt-rotor configuration.

Simple theories for the behaviour of rotors, for instance those based on momentum theory, are strictly invalid during slow descending flight. Although simple actuator disk theory has recently been revisited to account for the VRS by Spalart (2003), and theoretical studies of the dynamics of helical vortices have been conducted for many years now (Widnall 1972), computation of the VRS has only been attempted relatively recently. Numerical investigations of the VRS have been conducted using free-wake modelling (Bhagwat & Leishman 2000; Leishman, Bhagwat & Ananthan 2002) and detailed computational fluid dynamics (CFD) (Newman *et al.* 2003; Brown, Line & Ahlin 2004). Studies have focused on the role of the natural instability of the vortical wake of the rotor on the onset of the VRS. Using a linearized stability analysis of a computed helicoidal vortex wake, Bhagwat & Leishman (2000) and Leishman *et al.* (2002) showed that the rotor wake is inherently unstable, but that, for small descent rates, the rate of growth of perturbations to the wake structure increases as the descent rate of the rotor is increased. While the observation that the flow field of the descending rotor is unstable is an important one, a linear stability analysis cannot describe fully the highly nonlinear process by which the helicoidal rotor wake evolves into the toroidal configuration found in the VRS. Newman *et al.* (2003) and Brown *et al.* (2004) used a fully nonlinear time-dependent CFD model to study the development of the rotor wake near to the onset of the VRS. They showed that, under normal flight conditions, disturbances produced as a result of the instability of the rotor wake are simply convected away into the flow downstream of the rotor. As the descent rate of the rotor approaches the onset of the VRS, however, the point at which these disturbances reach appreciable magnitude moves up the wake towards the rotor. They postulated that nonlinear coupling between the loading produced on

the rotor and the flow perturbations produced by these disturbances eventually drives a global destabilization of the helicoidal rotor wake, resulting in the toroidal wake topology found in the VRS.

Current understanding of the behaviour of the rotor wake in the VRS is still incomplete, however. In particular, there is little direct experimental support for the numerical calculations showing how the flow field undergoes the transition into the VRS. While there exists a large amount of data regarding rotor performance in the VRS, there is a lack of detailed experimental data for the flow field of the rotor in the VRS. Given that the physics of the VRS is driven by the development of the rotor flow field, a detailed visualization of the development of the rotor flow under conditions near the onset of the VRS, using up-to-date experimental techniques, has the potential to shed further light on the VRS phenomenon, to guide theoretical analysis, and to provide validation data for CFD simulations. In this paper, results and analysis of a set of measurements of an experimental simulation of the VRS using a rigid rotor in simulated descent are presented. The main advantage of the PIV technique used to obtain the results presented in this paper is that it is able to resolve simultaneously the state of relatively large areas of the unsteady flow surrounding the rotor compared to other flow-visualization techniques. This is important when studying rotor flows in the VRS because of the extended nature of the spatial and temporal correlations in the flow. A certain descent rate is encountered where a very definite change in the character of the mean flow field near the rotor takes place. This observation suggests that a practical indicator of the onset of the VRS is the appearance of a large toroidal area of recirculation in the mean flow at or close to the rotor (as in Drees & Hendal 1951; Leishman *et al.* 2002), and that such an indicator might supplement other definitions for the onset of the VRS, such as the onset of thrust fluctuations as used elsewhere (Newman *et al.* 2003). At descent rates just below those where the fully developed VRS flow field is observed, the flow is highly unsteady, and analysis of the PIV results shows that in this incipient flow regime, the topology of the flow fluctuates intermittently between the down-flow topology found at lower descent rates and the flow topology found in the fully developed VRS.

2. Experimental method

2.1. *Description of apparatus*

An experimental simulation of a rotor in axial descent was performed by placing a three-bladed rotor of radius $R = 7.5\,\mathrm{cm}$ in a wind tunnel, with the rotor shaft parallel to the flow direction in the wind tunnel. The chord, thickness and blade pitch distribution along the rotor blades is shown in figure 1. The rotor was arranged to induce a velocity in the opposite direction to the wind-tunnel flow so that the wind-tunnel speed U_∞ could be used to represent the rotor 'descent speed' V_d. The wind tunnel used was a low-speed closed-return tunnel with a working section of $1.15\,\mathrm{m} \times 0.85\,\mathrm{m}$ and a turbulence level of approximately 0.3 %. Results were obtained for a range of wind-tunnel speeds from $0\,\mathrm{m\,s^{-1}}$ (representing hover) to $13\,\mathrm{m\,s^{-1}}$, and the rotor was run at a rotational speed of 120 Hz for all the tests, giving a tip speed of $V_{tip} = 56.5\,\mathrm{m\,s^{-1}}$. The feathering angle of the blades of the rotor could not be varied, thus it is important to note that all results presented in this paper pertain to the particular case of a rotor with approximatey 20° of blade twist run at a constant collective pitch of approximately 12° (as measured at the 3/4 blade radius). The Reynolds number, based on the geometric mean chord of the blade and the tip velocity, is 46 000. Tests of the rotor performance in hover showed no change of thrust

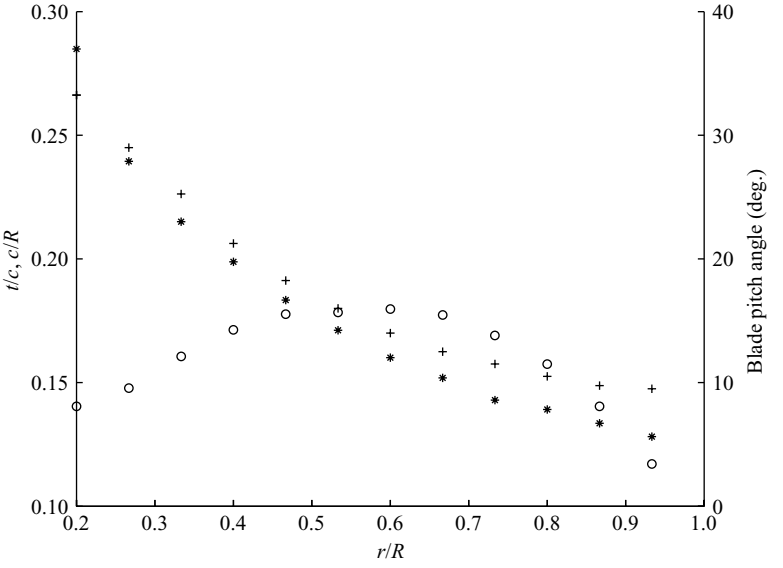

FIGURE 1. Chord, thickness and pitch profile of rotor blade. *, thickness, t; ○, chord, c; +, blade pitch.

coefficient across a wide range of rotational speeds, and the power consumed showed no unexpected variations. Furthermore, as the descent rate increased, the mean thrust varied in the manner expected for constant collective with constant rotational speed, and the power was only observed to rise when the descent rate reached a very high value. Therefore, significant and adverse viscous effects were not present within the experiment.

The rotor was powered by a d.c. electric motor (2 cm in diameter and 4 cm long), which was mounted at the end of a slender stiff horizontal sting (2.5 rotor diameters long) fastened rigidly to a faired support bolted to the wind-tunnel floor. The spindle connecting the rotor to the motor was kept short to minimize vibration, and an optical detector was used to measure the rotor's rotational speed. A diagram of the rotor is shown in figure 2. For later reference, an (x, y)-coordinate system, with its origin at the rotor hub is defined such that, for a descending rotor, the y-axis is vertically upwards and the x-axis is in the plane of the rotor.

The PIV system used for the current set of measurements was based on two Spectra-Physics Lab-130-10 double-pulsed frequency-doubled Nd:YAG lasers for illumination and two Kodak Megaplus ES1.0 digital video cameras operating in triggered double-exposure mode for photography. The laser repetition rate was 10 Hz, and the inter-pulse separation for each laser was set to 100 μs. The two laser beams were aligned with one another using a Brewster plate beam combiner, and the light sheet was delivered into the wind-tunnel working section from above using beam shaping optics, mirrors and a cylindrical lens. Each camera was fitted with Nikkor 50 mm f/2.8 lenses which were set to f/4 during the experiment. Each camera was synchronized with its own laser to 1 μs accuracy using a National Instruments PC-TIO-10 counter timer, and the digital images were captured using two National Instruments PCI-1424 digital image frame grabbers (one per camera). This PIV system was used in two ways to permit a thorough investigation of the flow field. Either one camera was used with one laser in a basic PIV mode, or two cameras were used with two lasers in a dual PIV mode

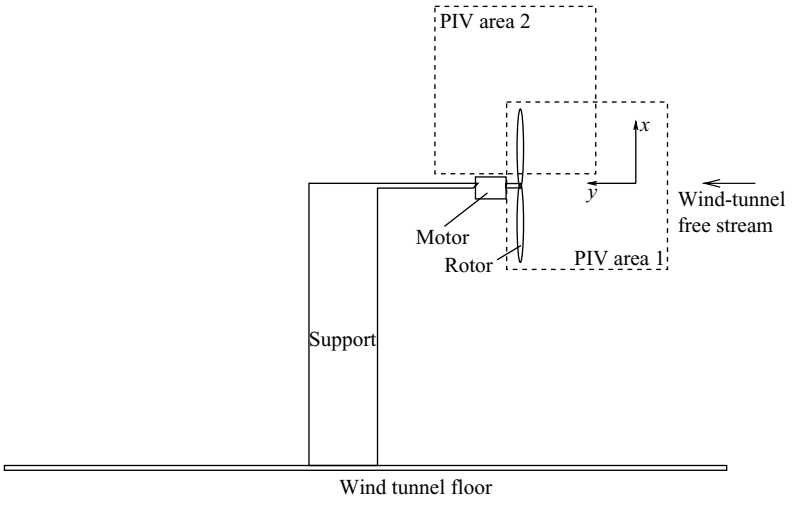

FIGURE 2. Schematic diagram of rotor rig in wind tunnel. The wind-tunnel free stream is from right to left, and the rotor induced velocity is from left to right. The rotor coordinate system is shown displaced from its origin at the rotor hub.

(to record the velocity field of the same area of the flow at two closely spaced time intervals). In the latter mode, the camera lenses were fitted with polarizing filters to prevent each camera from recording the pulse from the other camera's laser. This method has been used successfully before by Green, Doolan & Cannon (2002) to record the development of transient flows. Seeding for the PIV system was generated by a C. F. Taylor scientific smoke generator, which used an electrical heater to heat Shell Ondina EL oil to form a fine mist which was then pumped slowly into the wind tunnel using carbon dioxide. The nominal mist particle diameter was 2 μm.

Each camera was trained on an $18\,\mathrm{cm} \times 18\,\mathrm{cm}$ square area in the flow. As a compromise between the resolution of the flow and the spatial extent of the resolved domain, the flow near the rotor was partitioned into two separate PIV interrogation areas, as shown in figure 2. One interrogation area was positioned specifically to resolve the complexities of the flow below the rotor, while the other focused on the region outboard and above the descending rotor to provide a more global view of the development of the flow.

2.2. *PIV analysis methodology and accuracy*

After image capture, the raw images were analysed using the well-established cross-correlation based procedure for PIV. Where possible, the cross-correlation calculations were speeded up using the fast Fourier transform algorithm. Image sub-areas (tiles) of 32 pixels × 32 pixels were used for the PIV analysis. This resolution is equivalent to $0.067R \times 0.067R$, which is sufficient to be able to pick out small details such as the individual vortex cores in the flow. The forward–reverse tile test scheme (FRTT) described in Green *et al.* (2002) was used for validation of individual velocity vectors. Post-processing of the velocity vector map, to remove any false vectors not detected by the FRTT, was performed using a local vector map coherence method (Noguiera, Lecuona & Rodriguez 1997). The magnification of the PIV system tended to compound the occurrence of peak-locking on the vector maps, but no anti-peak-locking algorithm was employed in the PIV analysis. From previous calibration of

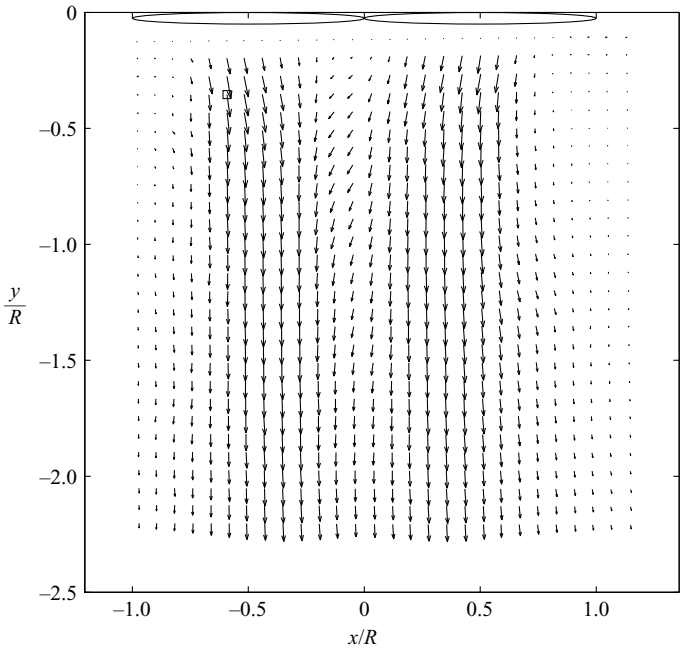

FIGURE 3. Mean flow field below rotor in hover. The maximum magnitude velocity vector is indicated by the box symbol at $v_i/v_h = 2.92$.

the PIV system, the accuracy of a well-validated velocity vector was known to be better than 3 %, however.

The measured instantaneous velocity data were post-processed to provide the instantaneous vorticity distribution in the flow (using the circulation method) as well as the mean velocity of the flow. The unsteadiness of the flow field was estimated by calculating the root-mean-square (RMS) fluctuation of the measured local unsteady velocity magnitude around the local mean velocity magnitude, defined as $\sqrt{\overline{u^2 + v^2} - \bar{u}^2 - \bar{v}^2}$. All the statistics (mean flow field and RMS) were calculated from approximately 120 velocity vector maps, thus providing good confidence limits to the data.

3. PIV results

3.1. *The flow field of the hovering rotor*

The hover case is important since the average induced velocity at the rotor disk can be used to scale the rotor descent rate, allowing the cases with the rotor in descent to be presented in a universal format. The mean velocity field below the rotor in hover is shown in figure 3. As expected, the results show the rotor to induce a significant downwash, concentrated in a stream tube extending into the flow below the rotor. The vector map is not completely symmetrical. Comparison of the velocity fields on either side of the rotor axis shows that the asymmetry is in fact confined to the velocity component in the direction away from the rotor axis. The mean velocity of this component for one half of the rotor is only 0.4 % of the mean down-flow component for the same half of the rotor. The asymmetry is therefore slight, and is due to an accumulation of small alignment errors of the laser sheet, rotor and wind-tunnel axis, a small degree of flow angularity in the wind tunnel and the natural swirl associated

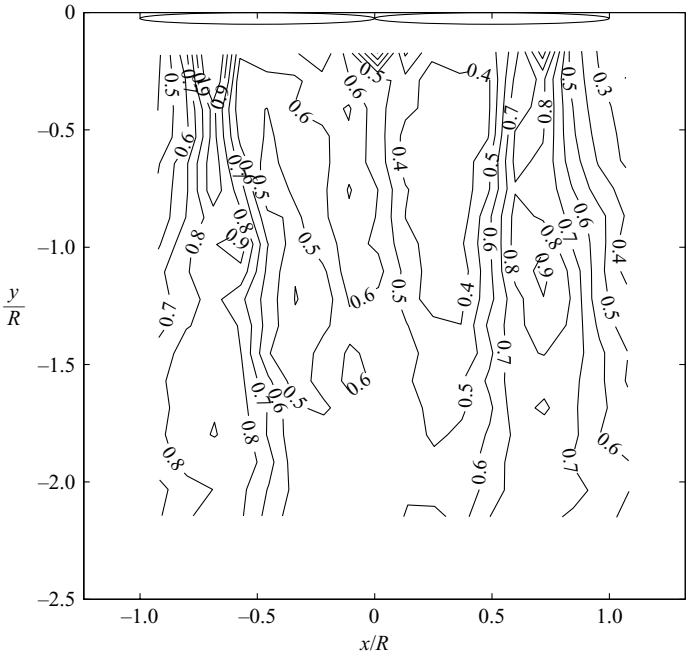

FIGURE 4. Root mean square of velocity field in hover. The values are scaled with v_h. The zones of highest RMS velocity are observed along tracks extending below the blade tips.

with the rotor rotation. While the alignment procedures were performed as carefully as possible, the observed result is consistent with the expected errors in the system. The velocity reaches a maximum magnitude of $v_i = 7.6\,\mathrm{m\,s^{-1}}$ just below the rotor, at the position indicated on the figure. The (mass flow) averaged induced velocity inferred from the PIV just below the rotor is $v_i = 2.4\,\mathrm{m\,s^{-1}}$. The thrust generated by the rotor was measured using a load cell, giving a thrust coefficient $C_T = T/\rho A V_{tip}^2 = 0.0043$. Standard momentum theory (see, for example, Leishman 2000) yields an induced velocity at the rotor disk of $v_h = \sqrt{C_T/2}\ V_{tip} = 2.6\,\mathrm{m\,s^{-1}}$, which agrees well with the average induced velocity inferred from the PIV. Figure 4 shows the associated unsteadiness in the velocity field. In general, the RMS fluctuation of the velocity signal is low, implying a relatively steady flow field throughout. As expected, though, there is a band of higher-velocity fluctuations extending downwards into the flow from just inboard of the rotor blade tips, and this is most probably associated with the passage of discrete tip vortices from each of the rotor blades as they roll up and convect away from the rotor along the edges of the wake streamtube.

3.2. *Effect of descent rate on the mean velocity field*

Figure 5 shows the development of the mean velocity field below the rotor as the descent rate is increased from hover to $V_d/v_h = 1.92$ ($V_d/V_{tip} = 0.089$). As the descent rate is increased, the hover-like flow pattern close to the rotor is increasingly encroached upon by a region of upwards flow further below the rotor. At the boundary between the upwards and downwards-moving flows, the velocity vectors turn sharply outwards away from the rotor axis, and the axial component of the velocity decreases

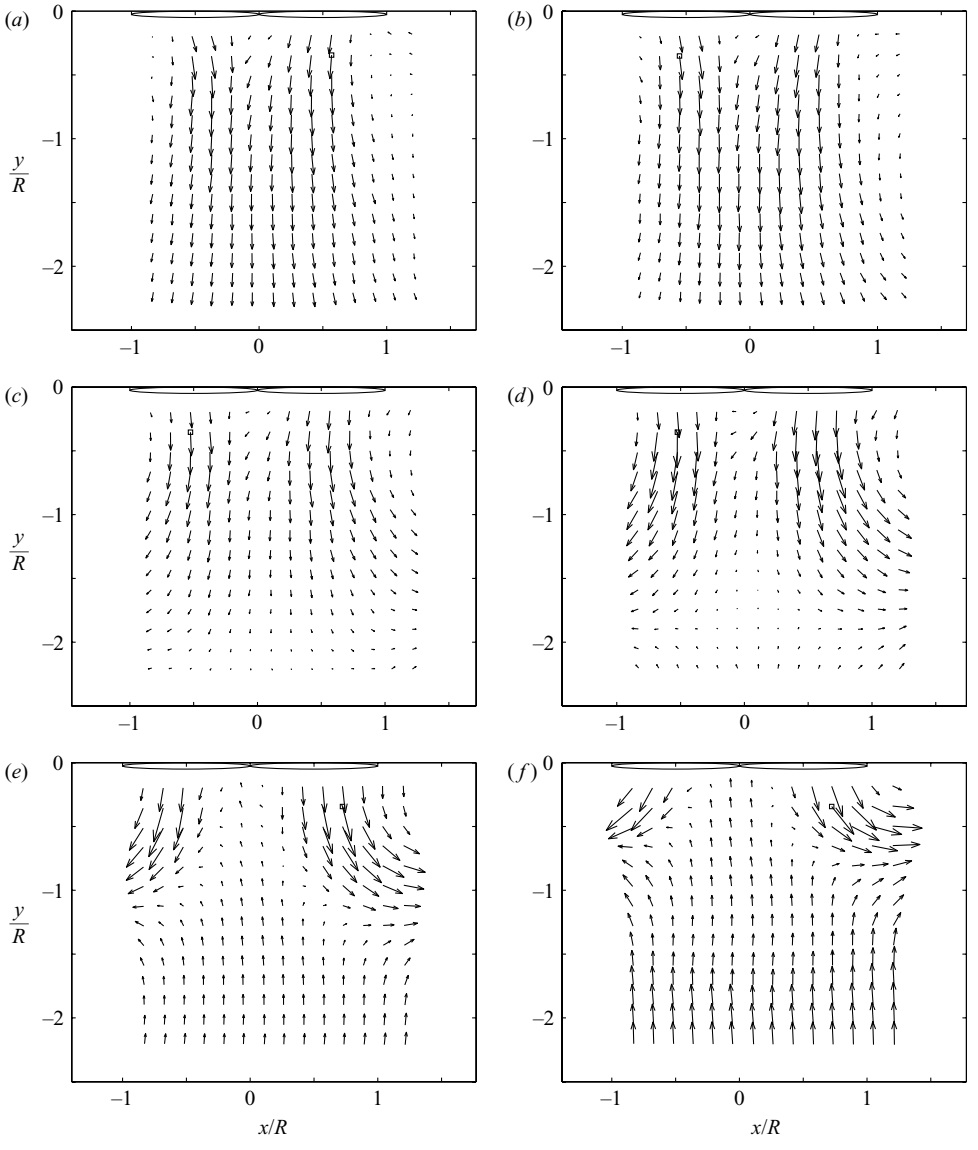

FIGURE 5. Development of mean velocity field below rotor as descent rate increases. Only a quarter of the velocity vectors are shown for clarity. Note the up-flow just below the disk in (*e*) and (*f*) (*a*) $V_d/v_h = 0.77$; (*b*) 1.25; (*c*) 1.35; (*d*) 1.44; (*e*) 1.54; (*f*) 1.92.

significantly – to the extent that, as shown in figures 5(*c*) and 5(*d*), a saddle point† in the mean flow enters into the PIV interrogation area, crossing its lower boundary when $V_d/v_h = 1.35$ and moving to roughly $1.75R$ below the rotor disk by the time $V_d/v_h = 1.44$. A marked change in flow topology accompanies a further increase in descent rate. The saddle point is no longer visible in the interrogation area at

† The authors use this terminology since in a highly unsteady field the existence of a stagnation point in the flow requires more stringent conditions on the mean flow than can be inferred from the data presented here.

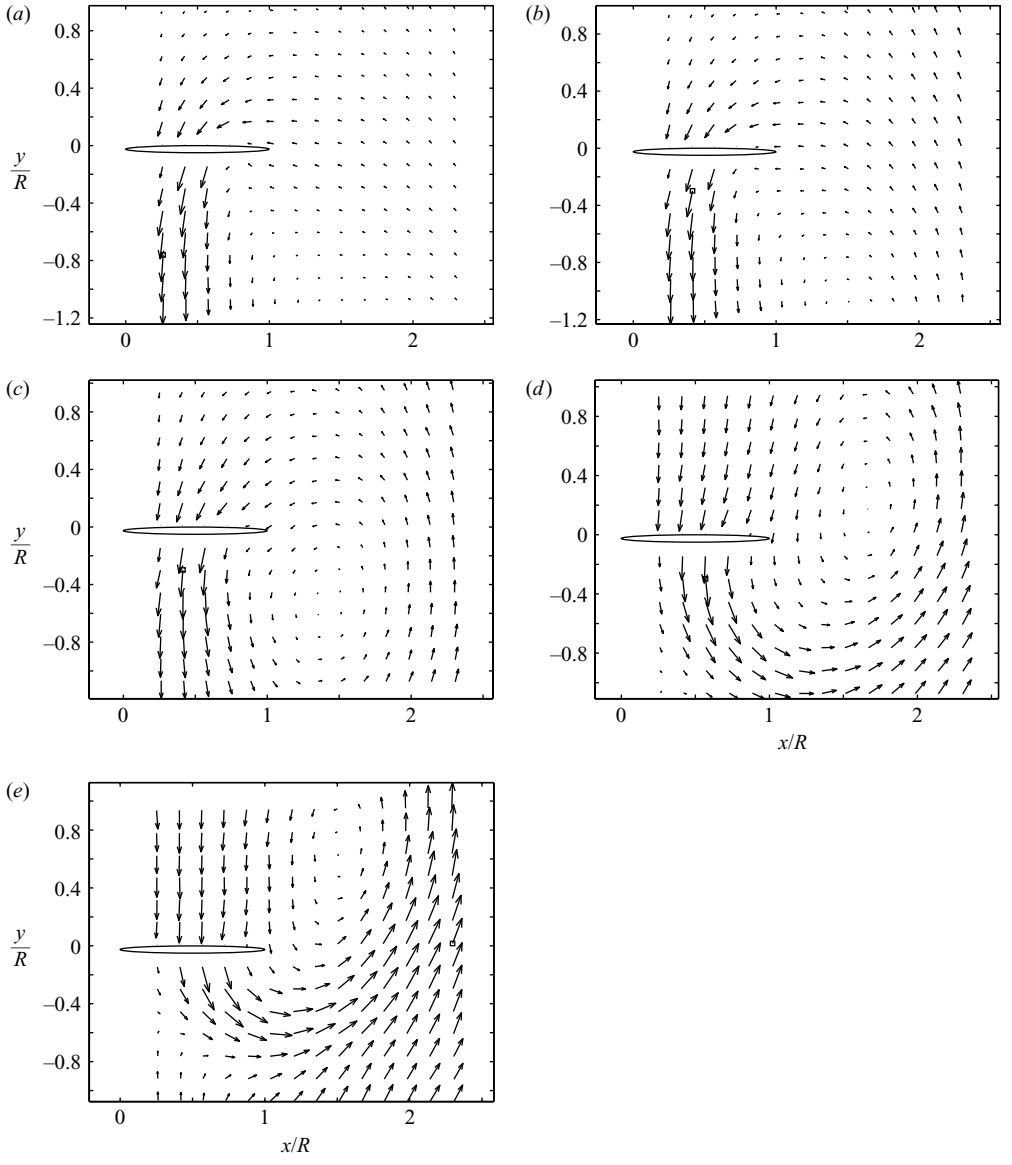

FIGURE 6. Development of mean velocity field around rotor tip as descent rate increases. Only a quarter of the velocity vectors are shown for clarity. Note how the recirculation zone in (*c*) moves to above the rotor disk in (*d*) and (*e*). (*a*) $V_d/v_h = 0.77$; (*b*) 1.15; (*c*) 1.35; (*d*) 1.54; (*e*) 1.92.

a descent rate $V_d/v_h = 1.54$ and, as shown in figures 5(*e*) and 5(*f*), a cone-shaped region of upwards flow penetrates all the way up to, and possibly through, the rotor disk. Unfortunately, figure 6, illustrating the development of the mean flow outboard on the rotor, does not show the flow close enough to the rotor axis for the fate of the saddle point to be ascertained. On the other hand, this figure does show the outwards displacement of the velocity vectors near the axis of the rotor to be associated with the development of a region of recirculating flow outboard of the rotor disk as the descent rate of the rotor is increased. At a descent rate $V_d/v_h = 1.15$,

the centre of this recirculation crosses the lower boundary into the outboard PIV interrogation area, and, as the descent rate of the rotor is further increased, the centre of the recirculation moves upwards and outwards until, at a descent rate $V_d/v_h = 1.92$, it lies approximately $0.6R$ above the rotor and $0.5R$ outboard of the rotor tip. Accompanying this motion is an obvious and significant increase in the mean velocity within the recirculating region of the flow.

3.3. *Effect of descent rate on the unsteadiness in the flow field*

Figures 7 and 8 show contour plots of the RMS fluctuation of the local velocity about the local mean, non-dimensionalized with respect to v_h. Whereas in hover the highest RMS values were concentrated in two almost parallel tracks extending from the rotor tips to the lower boundary of the PIV interrogation zone, as soon as the rotor enters descent these tracks broaden and diffuse laterally and do not extend as far into the flow below the rotor as before. This can be seen particularly in the images of figure 8 for descent rates $V_d/v_h < 1.35$. As the descent rate is further increased, these tracks narrow once more to form distinct arc-shaped bands of high RMS fluctuations in the velocity field extending out from under the rotor tips into the flow above the rotor. An interesting change in the structure of the RMS signal accompanies the appearance of the saddle point in the mean flow below the rotor, however. When the saddle point is present close to the rotor, the highest RMS values are no longer found near the rotor tips, but below the rotor in a large, spherical zone enclosing the saddle point. As the saddle point moves upwards towards the rotor, this spherical region of high RMS intensity moves with it. The disappearance of the saddle point marks a return to an unsteady flow field dominated by the structures generated at the tips of the rotor. Indeed, the presence of the saddle point in the mean flow correlates well with the peak values of the RMS velocity fluctuation measured in the flow. Figure 9 shows the mean RMS velocity fluctuation over the imaged flow field below the rotor, and the RMS level sampled at the rotor centreline at $2R$ below the rotor, both as a function of descent rate. Both curves follow a similar trend, and show a monotonic increase in the unsteadiness of the velocity field as the saddle point moves upwards towards the rotor, followed by a sharp decline at the descent rate at which the saddle point disappears from the PIV interrogation area.

Further insight into the detailed structure of the fluctuations in the flow can be obtained by performing a proper orthogonal decomposition (POD) of individual PIV snapshots of the flow. Using this approach, any underlying structure to the fluctuations can be found by decomposing the flow in terms of a set of basis modes that are optimal in the sense that the first M modes contain the greatest possible proportion of the kinetic energy present in the flow. The technique is applied as follows. In this experiment, the data for each PIV velocity field consists of $x-$ and $y-$ velocity components at 18×18 points in the flow and so may be represented by a vector $\boldsymbol{v}$ of 648 elements. At any particular descent velocity, given an ensemble of N different PIV snapshots, the correlation matrix of the fluctuating flow, $\boldsymbol{v}' = \boldsymbol{v} - \bar{\boldsymbol{v}}$, is given by

$$\boldsymbol{R} = \frac{1}{N} \sum_{i=1}^{N} \boldsymbol{v}'^{T}_{i} \boldsymbol{v}'_{i}$$

where $\bar{\boldsymbol{v}}$ is the average velocity field. The basis modes that characterize the fluctuating structures in the experimental data are then the eigenvectors of this matrix. The relative significance of each mode in encapsulating the fluctuations in the flow is judged by its eigenvalue. At each descent rate, the eigenvalue λ_i of the correlation

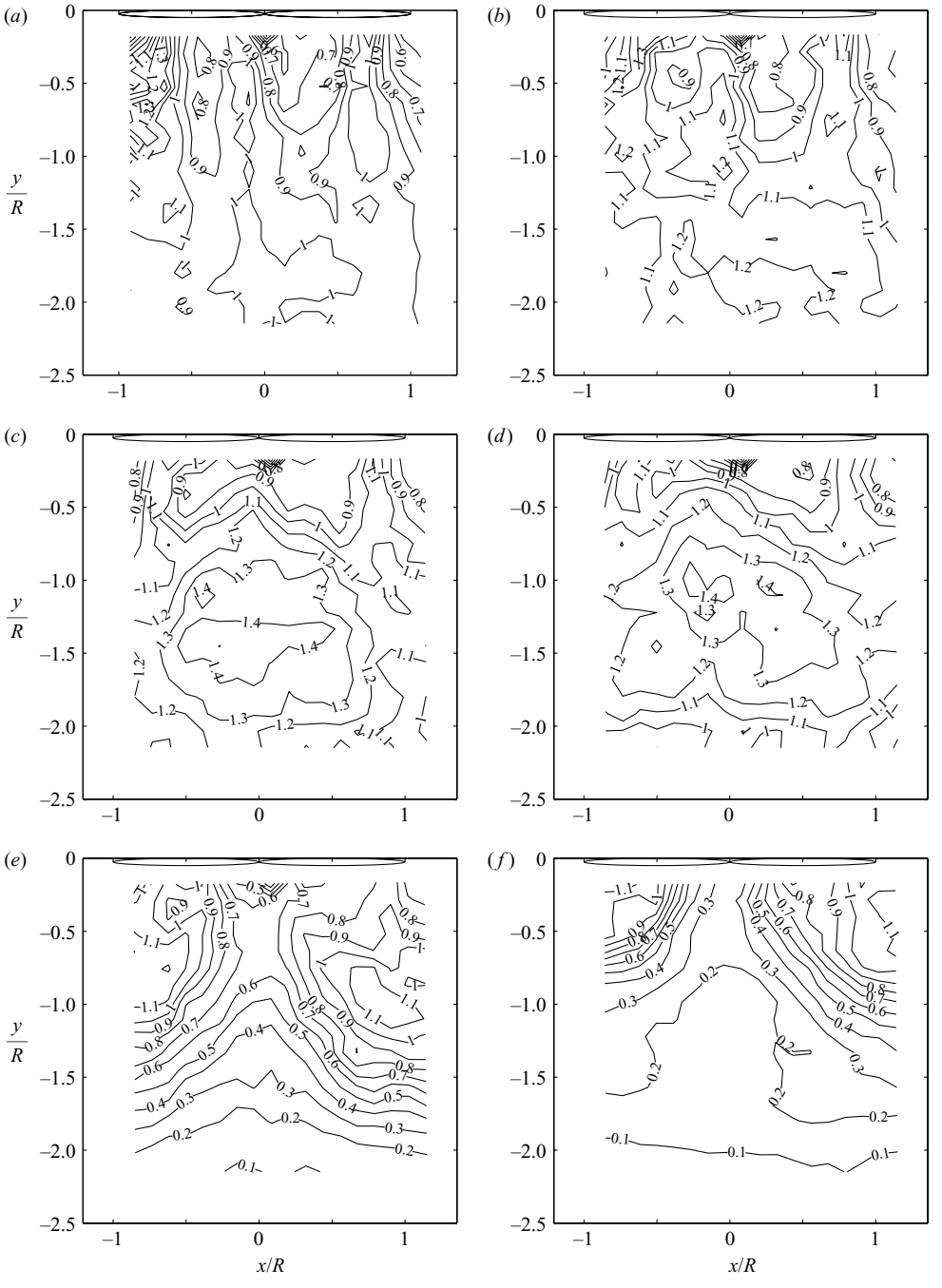

FIGURE 7. Development of the RMS velocity field below the rotor as descent rate increases. The values are scaled with v_h. In (*c*) and (*d*) the RMS velocity reaches a maximum overall level. (*a*) $V_d/v_h = 0.77$; (*b*) 1.25; (*c*) 1.35; (*d*) 1.44; (*e*) 1.54; (*f*) 1.92.

R is normalized by the sum of all other eigenvalues at that descent rate, such that $\Lambda_i = \lambda_i / \sum \lambda$. The normalized eigenvalue therefore quantifies the probability of occurrence of that mode in the fluctuating flow (if the data were three-dimensional and

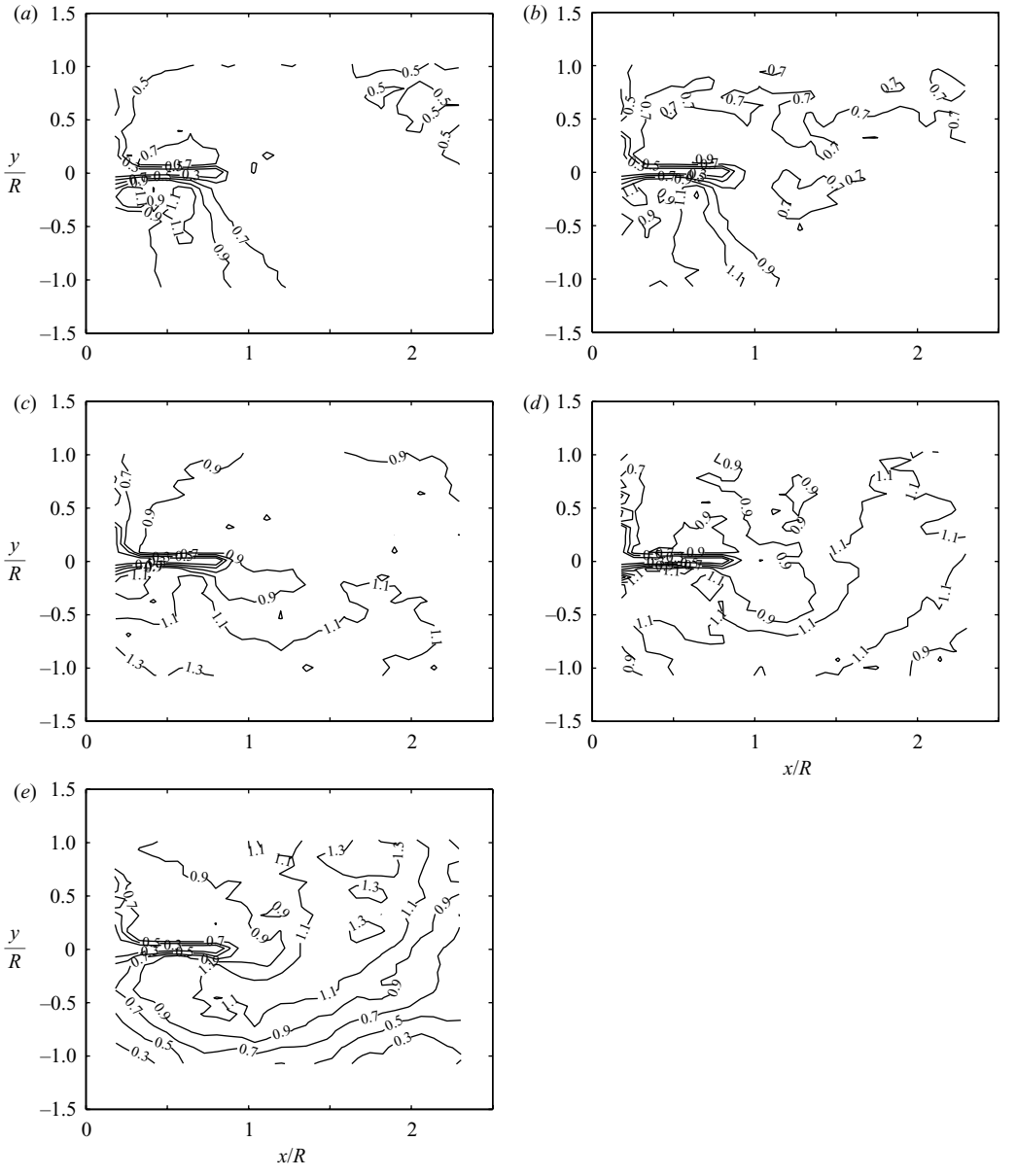

FIGURE 8. Development of the RMS velocity field around the rotor tip as the descent rate increases. The values are scaled with v_h. As the descent rate increases, the high RMS zone migrates from below the rotor disk to above it. (*a*) $V_d/v_h = 0.77$; (*b*) 1.15; (*c*) 1.35; (*d*) 1.54; (*e*) 1.92.

continuous, the eigenvalues would represent the fraction of kinetic energy accounted for by the modes, Glezer, Kadioglu & Pearlstein 1989).

The POD† of the flow at the pre-VRS descent rate $V_d/v_h = 1.25$ shows a single dominant large-scale mode having a normalized eigenvalue of $\Lambda_1 = 0.19$, with all

† Note that the POD correlation matrices at $V_d/v_h = 1.25$, 1.44 and 1.54 were obtained using, respectively, 104, 120 and 120 individual PIV snapshots of the flow.

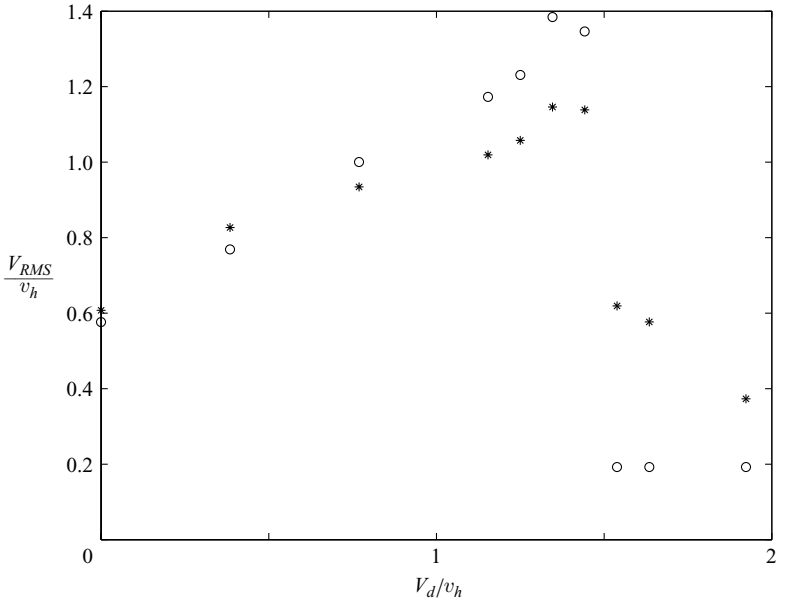

FIGURE 9. Peak and spatially averaged RMS velocity levels observed below rotor. The peak RMS levels are taken from $2R$ below the rotor disk. ○, peak RMS level $2R$ below rotor; ∗, mean RMS level.

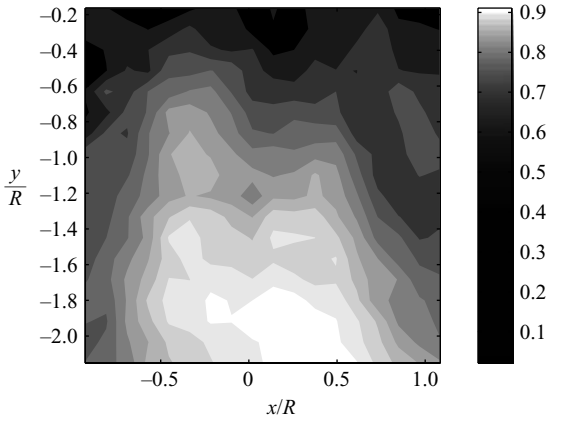

FIGURE 10. Most energetic POD mode at descent velocity $V_d/v_h = 1.25$; shown are normalized contours of velocity magnitude of equal spacing.

higher modes at this descent velocity consisting of much smaller scales. As shown in figure 10, this first mode occupies the same large spatially extended spherical area well below the rotor as was identified in the RMS velocity data for this descent rate.

At the intermediate descent rate $V_d/v_h = 1.44$, the first POD mode for the flow is structurally similar to the first mode observed at $V_d/v_h = 1.25$, as shown in figure 11. The normalized eigenvalue of the new first mode is $\Lambda_1 = 0.42$, more than twice that at the lower descent rate. This descent rate is characterized by the appearance of two other competing fluctuation modes. These secondary modes have roughly similar normalized eigenvalues to each other, having $\Lambda_2 = 0.06$ and $\Lambda_3 = 0.07$. As shown in

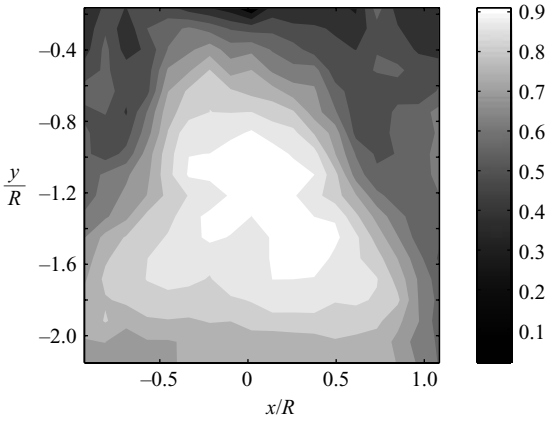

FIGURE 11. First POD mode at descent velocity $V_d/v_h = 1.44$; shown are normalized contours of velocity magnitude of equal spacing.

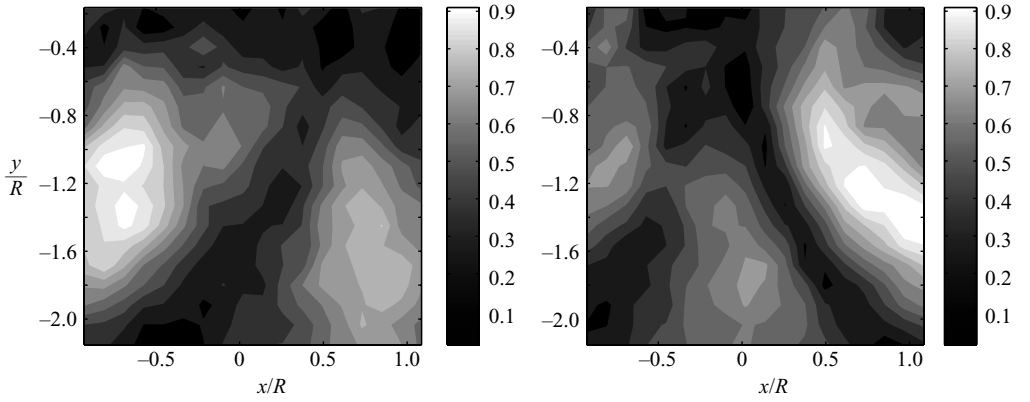

FIGURE 12. Second and third POD modes at descent velocity $V_d/v_h = 1.44$; shown are normalized contours of velocity magnitude of equal spacing.

figure 12, these modes describe a set of velocity fluctuations with energy content concentrated along arc-shaped trajectories lying some distance below the rotor – with the maximum energy distributed in much the same location as the recirculation zones visible in the corresponding mean flow image of figure 5. Although these modes might be described as crude mirror images of each other about the rotor axis, both show a significant division of energy between the left-hand and right-hand sides of the rotor. However, a linear combination of these modes, multiplied by their respective eigenvalues, is almost symmetrical about the rotor axis.

As the descent rate of the rotor is further increased, the spherical mode disappears and the fluctuations in the flow field are dominated by the arc-shaped modes lying below the rotor. At a descent rate $V_d/v_h = 1.54$, these modes have normalized eigenvalues of $\Lambda_1 = 0.20$ and $\Lambda_2 = 0.15$ and, as shown in figure 13, are now concentrated somewhat closer to the edge of the rotor disk. At this descent rate, this pair of modes shows a distinct geometrical mirror symmetry about the rotor axis. This indicates that fluctuations in the flow field below the rotor, at this descent rate, are either axisymmetric, with both POD modes in approximately equal combination, or asymmetric with fluctuations concentrated over a smaller range of azimuth.

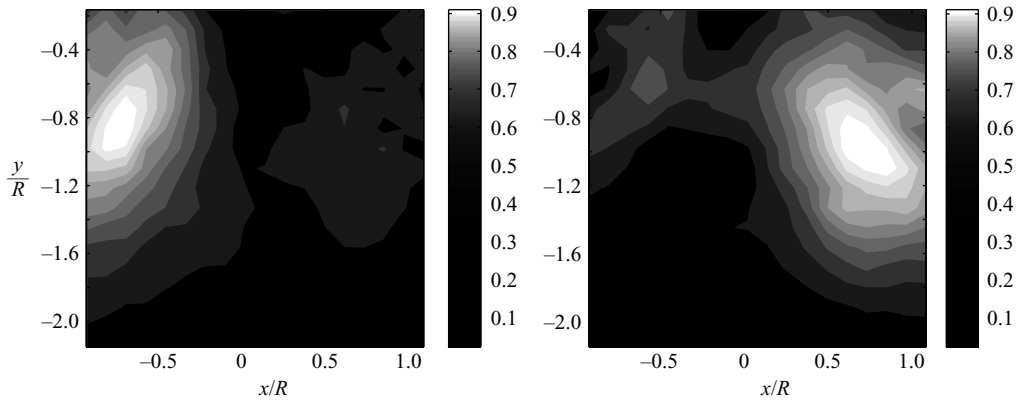

FIGURE 13. First pair of POD modes at descent velocity $V_d/v_h = 1.54$; shown are normalized contours of velocity magnitude of equal spacing.

3.4. *Measurements of the vorticity field near the rotor*

Figure 14 shows a series of individual PIV snapshots of the vorticity field near the rotor over a range of descent rates to help ascertain the origin of the unsteadiness in the flow field. These snapshots were selected to be characteristic of the flow at the various descent rates already shown in figures 6 and 8. The diagrams show a set of concentrated vortex cores streaming from the rotor tips into the flow below the rotor, and the positions of the vortex cores correlate well with the locations of the bands of high RMS fluctuation in the velocity field discussed in the previous section. At the lowest descent rates (figures 14*a* and 14*b*), the position of the vortex cores is consistent with the presence of a tubular wake extending into the flow below the rotor. At higher descent rates, the vorticity plots show the disruption of this tubular wake as, rather than propagating downwards into the flow below the rotor, the vortex cores are increasingly swept laterally in a curved trajectory that loops back around the tips of the rotor and up into the flow above the rotor disk. Measurements using the dual PIV system show, indeed, that the vortex cores are eventually caught up in the zone of recirculating flow exposed by the measurements of the mean velocity of the flow field, but the eventual fate of the vortex cores is obscure. This is because the time-delay between successive dual mode PIV snapshots makes it impossible to identify the same individual vortex core in two successive sets of PIV images.

The flow situation observed at $V_d/v_h = 1.35$ is somewhat more complex than portrayed in figure 14(*c*). The vorticity pattern that is illustrated shows the more common situation at this descent rate where a set of vortex cores convects in an arc past the tips of the rotor and into the mean-flow recirculation zone that is located just below, and outboard of, the rotor disk. Other snapshots at the same descent rate show a pattern far more like that encountered at lower descent rates, however, with the concentrated vortices streaming vertically downwards into the flow below the rotor. The dual nature of the flow field at this descent rate appears to be an important contributor to the unsteadiness of the flow near the onset of the VRS, and this feature of the flow will be analysed in more detail later in this paper. As a final observation, it should be noted that none of the vorticity contour maps presented here explain the presence of the spherical zone of high RMS velocity fluctuation surrounding the saddle point below the rotor.

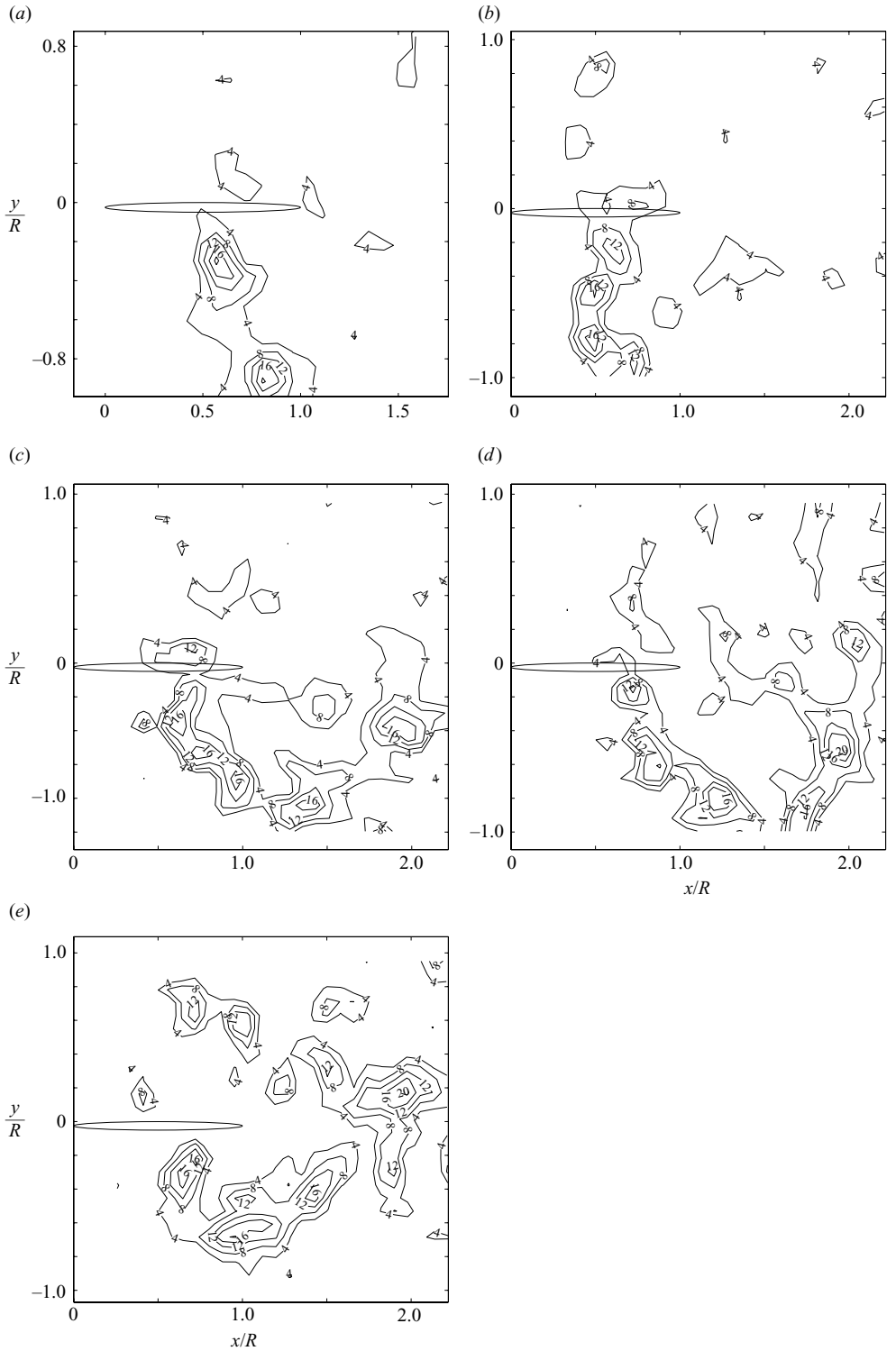

FIGURE 14. Development of the vorticity field around the rotor tip as the descent rate increases. Representative instantaneous vorticity plots are shown. The values are scaled with v_h/R. At the higher descent rates, the tip vortices accumulate in a small zone around the tip. (*a*) $V_d/v_h = 0.77$; (*b*) 1.15; (*c*) 1.35; (*d*) 1.54; (*e*) 1.92.

4. Discussion

The PIV results described in the previous section show the flow to change significantly as the descent rate of the rotor is increased away from hover. At very low descent rates, the data are consistent with the conventional picture of the rotor wake as consisting of a stream of helical tip vortices convecting down the boundary of a streamtube that extends downstream away from the rotor disk, and in which the flow is directed downwards away from the rotor.

As the descent rate of the rotor is increased, however, the classical picture of the wake as a simple streamtube becomes less appropriate as the results show the down-flow below the rotor to be replaced increasingly by a region in which the flow is directed upwards towards the rotor. At the same time, the tip-vortices no longer convect away into the flow below the rotor, but are deflected laterally into a zone of recirculation that initially forms some distance outboard and below the rotor disk. This zone of recirculation moves upwards and outwards until, at sufficiently high descent rate, it lies above the plane of the rotor. Extrapolating the planar PIV measurements into the third dimension, the results show a breakdown of the cylindrical wake of the rotor into a toroidal recirculating flow structure in a manner entirely consistent with the conventionally accepted notion of the onset of the VRS in the flow surrounding the rotor.

The appearance of the up-flow region below the rotor disk at low descent rates is similar to that observed during smoke-flow visualizations of a rotor in the VRS by Brinson & Ellenrieder (1998), and the data presented here support their suggestion that, at very low descent rates, the flow penetrates through the rotor over a small inboard area of the disk. Direct confirmation of their inference is not possible, however, since PIV measurements directly above the rotor centre are prevented by the presence of the shaft and motor. The presence of the saddle point in the mean flow appears to have gone unnoticed in previous studies, however – possibly because the feature appears only after post-processing of a flow which in essence is highly unsteady. (For instance, it is difficult to discern the positions of any equivalent points in the snapshots of the velocity field presented in figure 15.) Nevertheless, the identification of features such as this is important if the changes in the topology of the flow that occur near the onset of the VRS are to be understood. In this vein, some initial CFD simulations (Newman *et al.* 2004), replicating this experiment, support the existence of the saddle point in the mean flow, and show the penetration of the flow through the rotor to be associated with the passage of the saddle point through the rotor disk.

It is instructive to try to place these observations within the context of published data for the onset of VRS. Newman *et al.* (2003), and particularly Johnson (2004), have collated a wide range of historical data for the behaviour of rotors in the VRS. In comparing with these data, the discrepancy between a scaling velocity v_h based on the thrust measured on the rotor when hovering (as done here) and a scaling velocity based on the mean thrust generated by the rotor at the descent conditions of interest, as used in some previously published works, must be borne in mind – although this discrepancy amounts to less than 10 % at the descent rates of relevance here. The variation of RMS velocity magnitude presented in figure 9 correlates rather well with the variation with descent rate of the maximum thrust perturbation on the rotor observed by both Washizu *et al.* (1966) and Betzina (2001) (as reproduced in figures 31 and 32 of Johnson 2004). All data show the maximum fluctuations to occur within a band of descent rates between $V_d/v_h = 0.9$ and 1.4.

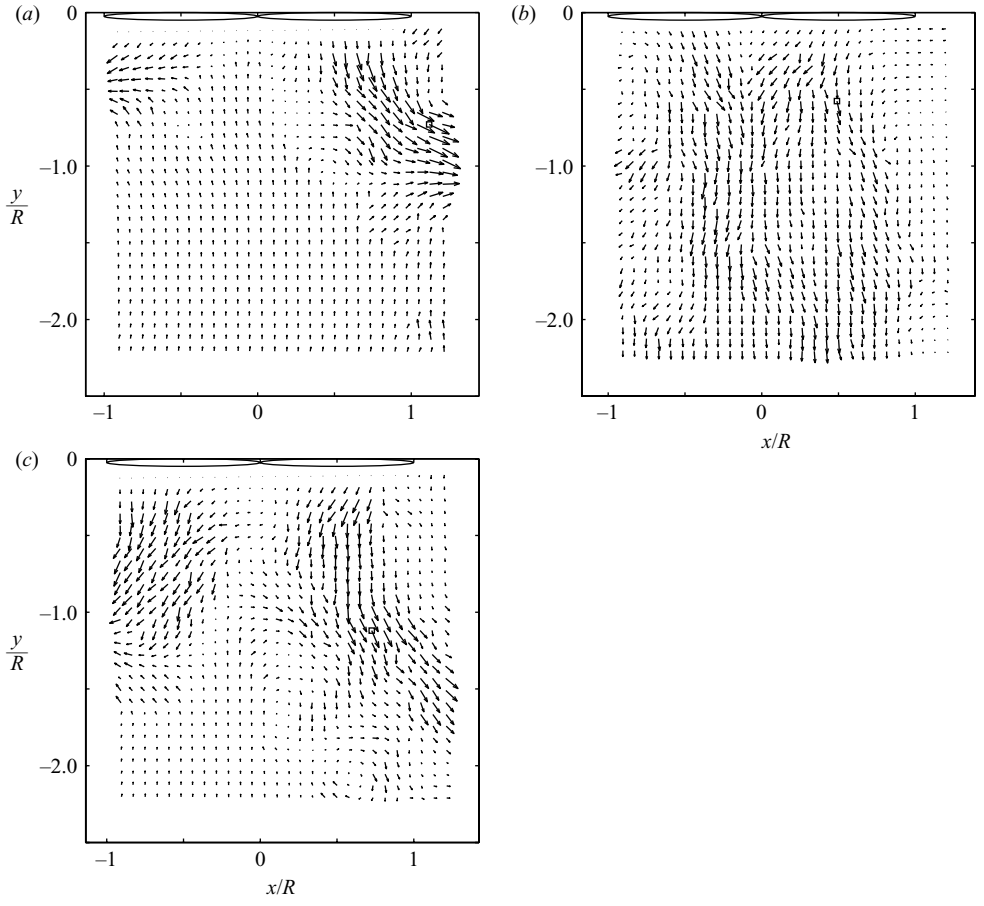

FIGURE 15. Typical individual velocity fields below the rotor for $V_d/v_h = 1.44$. (*a*) Up-flow, correlates well with the mean flow for $V_d/v_h = 1.54$, (*b*) down-flow, correlates well with the mean flow for $V_d/v_h = 1.25$, and (*c*) shows a typical asymmetric flow field.

The link between the fluctuations in the induced flow, or the rotor thrust, and the global behaviour of the rotor wake that must drive these fluctuations, has been poorly established in previous studies, however. The observations presented here suggest that the maximum unsteadiness in the flow does not occur within the range of descent rates over which the flow adopts the pattern that is classically associated with the vortex ring state. Instead, comparison of figure 9 and the PIV images of the mean flow shows the maximum unsteadiness to occur in the lead-up to a rather obvious and sudden change in the flow that marks the appearance of the classical vortex ring structure. This observation goes some way to explaining the wide variation in the measured descent rate for VRS onset (as shown, for instance, in figure 5 of Newman *et al.* 2003) when the onset of the VRS is judged by various, possibly incompatible, measures of the behaviour of the rotor system such as the amplitude of fluctuations in induced velocity or thrust coefficient, control difficulty, or the observed flow topology. The problems posed by this ambiguity in the definition of VRS onset are well illustrated by the PIV results presented both here and by Newman *et al.* (2003). In particular, although the descent rate for their VRS case was well within the range of descent rates associated with strong unsteadiness in the flow, the PIV

images presented by Newman *et al.* (2003) show an average down-flow below the rotor, which as they stated, bears a strong resemblance to the flow field found at hover. In particular, no evidence is visible of the flow recirculation close to the rotor that is classically associated with the VRS. These results support the inference from the data presented here that, while it might be practically expedient to define the VRS onset for a rotorcraft in terms of more easily accessible dynamic parameters than the state of the flow around the rotor, such a definition might not concur with any significant change in the global structure of the flow.

The change in the flow marking the appearance of the classical vortex ring structure takes place as the descent rate of the rotor is increased past a critical value of approximately $V_d/v_h = 1.35$. At this critical descent rate, the velocity field is at its most unsteady, and a small increase in descent rate results in a rapid upwards migration of the saddle point marking the division between the upwards and downwards flows below the rotor. This behaviour is accompanied by a simultaneous migration of the lateral recirculation zones from below to above the plane of the rotor, and a shift in the region of maximum unsteadiness in the flow from below the rotor to within the recirculation zones above the rotor disk.

Although results will be influenced strongly by the details of the rotor geometry, particularly the blade twist (Brown *et al.* 2002), the data presented here for the wake geometry when in the VRS are in broad qualitative agreement with flow visualizations presented elsewhere. The measurements of Drees & Hendal (1951) show a broadly similar recirculating flow around the rotor, although, in their images, the centre of the recirculation zone appears to lie inboard of the blade tips. The experiments of Drees & Hendal (1951) were conducted in non-axial flight and with a fuselage present, however. Similarly, Brinson & Ellenrieder (1998) also depict the recirculation to lie inboard of the blade tips, but this may be attributable to the rather high wind-tunnel blockage in their experiment. The flow-visualization results of Stack *et al.* (2004), however, were performed in a large water tank using a rotor with similar dimensions to that used in this study. Their results show a very similar placement of the recirculation zones at very similar values of descent rate compared to the current observations – although the images they provide are again for non-axial descent.

Based upon the observed changes in the topology of the flow field with descent rate, the experiment described in this paper can thus be interpreted as showing the development of the rotor wake starting from hover, progressing through the transition to VRS starting at about $V_d/v_h = 1.35$ and ending deep within the VRS as the descent rate is increased above $V_d/v_h = 1.54$. The remainder of the paper deals in somewhat more detail with the unsteady fluid dynamics of the rotor system near to the onset of the VRS.

4.1. *Mechanism of VRS onset*

At non-dimensional descent rates between 1.35 and 1.44 where the average RMS intensity of the velocity fluctuations below the rotor is the highest, successive snapshots of the velocity field below the rotor hint at significant global changes in the structure of the flow field as time progresses. The implication of this observation is that the increased unsteadiness in the flow below the rotor just prior to the onset of the VRS might result from large-scale spatially correlated changes in the flow pattern, rather than simply from an increase in the intensity of local fluctuations in the velocity field, for instance, as a result of the passage of strengthened individual vortex cores along an essentially time-invariant trajectory.

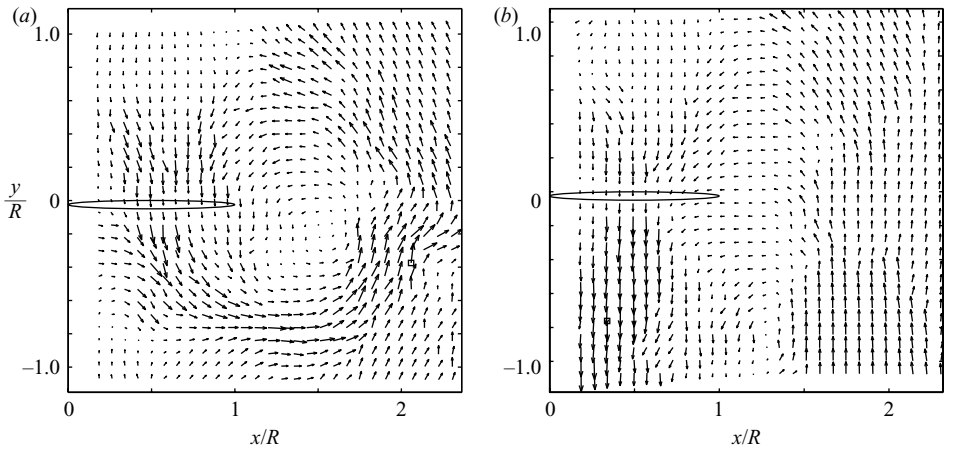

FIGURE 16. Typical individual velocity fields around the rotor tip for $V_d/v_h = 1.35$. (*a*) Up-flow, correlates well with the mean flow for $V_d/v_h = 1.54$ and (*b*) down-flow, correlates well with the mean flow for $V_d/v_h = 1.15$.

Closer inspection of the proper orthogonal decompositions of the fluctuations in the velocity field, presented in § 3.3, reveals an interesting fact. Prior to the onset of the VRS, the fluctuations in the flow are concentrated below the rotor in a spherical region lying along the axis of the rotor. Within the VRS, the fluctuations in the flow have a very different structure, and are concentrated in a pair of arc-shaped lobes that are laterally displaced with respect to the centreline of the rotor. Yet, within the critical regime just prior to VRS onset, the POD can be interpreted as showing that the unsteadiness in the flow results from the competition between two distinct modes: one of which is qualitatively very similar to the dominant fluctuation mode at pre-VRS descent rates, and the other of which is qualitatively very similar to the structure found well within the VRS.

Indeed, comparison of a large number of snapshots suggests that the flow within the critical range of descent rates between $V_d/v_h = 1.35$ and 1.44 might be alternating between two different states, one having a form very similar to the tubular structure observed at lower descent rates, and another having a form very similar to the toroidal structure found within the fully developed VRS. The maximum frame-rate of the basic PIV system was insufficient for the frequency of alternation of the flow structure to be determined, however, and pairs of consecutive snapshots obtained using this system show both similar and dissimilar topologies. Intermediate states showing varying degrees of up-flow and down-flow were also captured, and many snapshots showed a flow that was highly asymmetric with respect to the rotor axis. A representative sample of snapshots from below the rotor for $V_d/v_h = 1.44$, one showing a typical up-flow case reminiscent of the toroidal topology found in the VRS, another showing a more tubular down-flow case, and another showing a typical asymmetric case are shown in figure 15. Similar images from above the rotor are shown in figure 16. On the other hand, measurements using the dual PIV system showed that the wake evolves relatively slowly compared to the rotational period of the rotor, with no complete topological change ever being observed within less than three rotor revolutions. Given that some complete changes in flow topology were observed in consecutive snapshots obtained using the basic PIV system, and that one snapshot could be obtained every 12 rotor revolutions, it appears that the most extreme changes to the flow state might

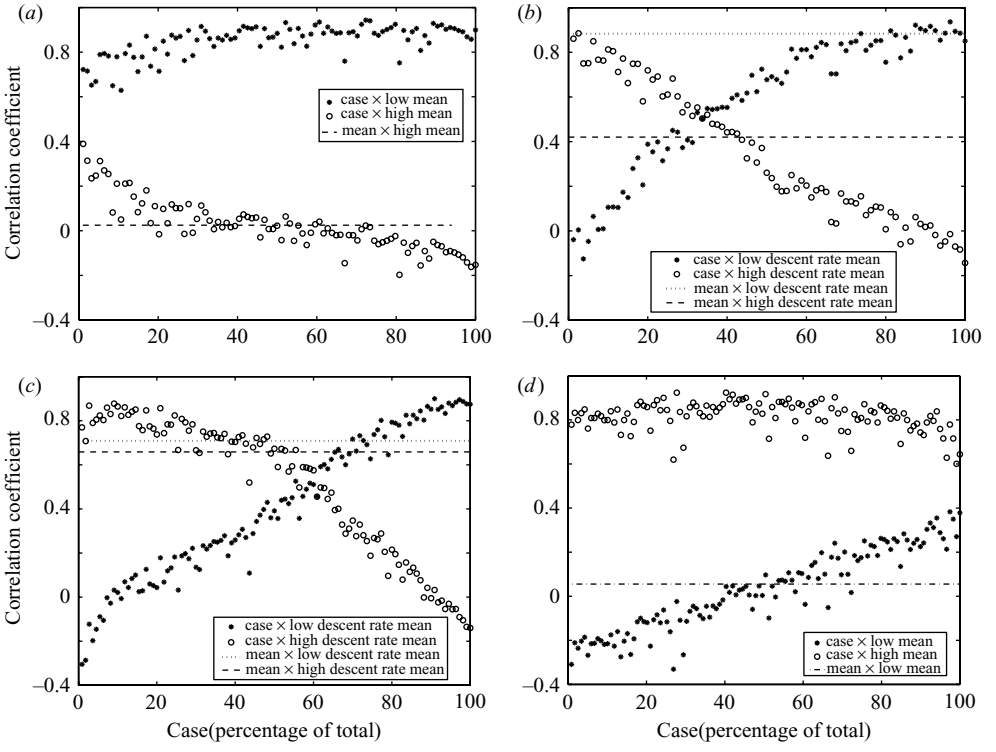

FIGURE 17. Correlation analysis of the individual velocity vector maps of data sets at intermediate descent rates with mean velocity fields at (*a*) $V_d/v_h = 1.25$, (*b*) 1.35, (*c*) 1.44, (*d*) 1.54.

require between three and twelve rotor revolutions to take place. This observation agrees well with Stack *et al.* (2004), who estimated a flow development period of 11 revolutions from measurements taken on their rotor in the VRS.

These rather qualitative observations regarding the alternating nature of the flow in incipient VRS can be put into a more objective framework by correlating the flow patterns observed at any particular instant against a set of 'prototype flows' that characterize the topology of the velocity field on either side of the critical range of descent rates. Figure 17 shows the results of such a correlation against the two prototype flows shown in figure 18. The prototype shown in figure 18(*a*), constructed from the mean flow at $V_d/v_h = 1.25$, is representative of the tubular flow topology found at subcritical descent rates, while the prototype shown in figure 18(*b*), constructed from the mean flow at $V_d/v_h = 1.54$, is representative of the topologically very different, toroidal mean flow found at supercritical descent rates within the VRS. In figure 18, the topology of the two prototype flows has been represented using integrated particle trajectories, and it should be mentioned that symmetry about the rotor axis has been enforced in these diagrams by averaging the mean flow at the appropriate descent rate with its reflection about the rotor axis. This was done to restore to the prototypes the symmetry that is obviously broken in the data presented in figure 5 – on the principle that, despite a small discrepancy that might be induced by the slight flow angularity in the wind tunnel, the flow observed in any snapshot should be equally as probable as its mirror image. The arrows on the plots indicate the local flow direction. An important check on the validity of these prototypes as descriptors of the flow was performed by confirming that the instantaneous

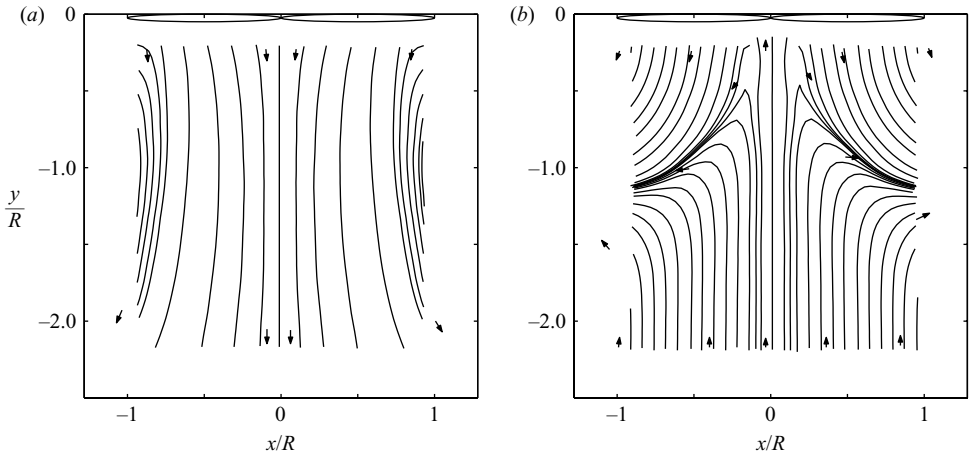

FIGURE 18. Prototypes for the flow topology in incipient VRS. (*a*) tubular flow, $V_d/v_h = 1.25$, (*b*) toroidal flow, $V_d/v_h = 1.54$.

velocity fields measured at $V_d/v_h = 1.25$ had very low correlation with the prototype constructed from the data obtained at $V_d/v_h = 1.54$, and vice versa. Indeed, direct inspection of the individual flow fields used to construct the prototypes showed that none of the snapshots obtained at the two different descent rates showed significant departure from the basic topology of their respective mean flows, as figure 17(*a*), at $V_d/v_h = 1.25$, and figure 17(*d*), at $V_d/v_h = 1.54$, show.

Figure 17(*b*) shows that, at lower descent rates within the critical regime (in this case $V_d/v_h = 1.35$), a significant number of the measured instantaneous velocity fields correlate well ('well' taken to mean a correlation coefficient above 0.75) with the tubular prototype for the flow at very low descent rates, but that relatively few correlate well with the toroidal prototype for the flow within the VRS. A comparison of figures 17(*b*) and 17(*c*) shows a distinct shift in the balance of the correlation as the descent rate of the rotor is increased towards the higher end of the critical regime. At $V_d/v_h = 1.44$, significantly more of the measured snapshots correlate well with the toroidal prototype flow than at $V_d/v_h = 1.35$, and fewer with the tubular prototype. Note though that, in both cases, a significant number of images correlate as well with the toroidal prototype as with the tubular prototype flow. Given a constant interval between successive snapshots of the flow, these observations are consistent with a flow that, over a critical range of descent rates just prior to the onset of the VRS, switches intermittently between having the tubular topology found at lower descent rates and the toroidal topology that is characteristic of the VRS. Furthermore, the correlation analysis suggests that the mechanism whereby the flow enters the VRS might involve an intermittency in the flow, in which the flow spends increasingly more time in the toroidal VRS-like form, with excursions back to the pre-VRS tubular form becoming less and less frequent, as the descent rate of the rotor is increased through the critical range of descent rates prior to the onset of VRS.

4.2. *Physical model for VRS onset*

These observations appear to be consistent with the description of the onset of the VRS in terms of the development and growth of instabilities in the rotor wake as put forward by Leishman *et al.* (2002), Brown *et al.* (2002) and Newman *et al.*

(2003). Well away from the onset of the VRS, the vorticity generated as a result of the aerodynamic loading on the rotor blades convects away from the rotor along a cylindrical streamtube that extends downstream into the flow below the rotor. It seems reasonable that, at low enough descent rates, the flow velocity in the streamtube is sufficient for any of the products of the natural instability of the rotor wake (see Leishman *et al.* 2002) to be swept away down the streamtube, from where they can have little influence on the development of the flow near the rotor. As the descent rate of the rotor is increased and the onset of the VRS is approached, it seems sensible, however, that this situation should begin to change. It seems natural that any structures generated by the instability of the rotor wake will be distributed over a range of strengths and length scales. Once the descent rate of the rotor is increased beyond a critical value, the largest and strongest of these disturbances would be capable of propagating up the rotor wake, occasionally disrupting the orderly generation of the streamtube – in this case, causing the wake to collapse into a recirculating strongly disordered flow.

The increasing frequency of excursions into a VRS-like flow state as the descent rate of the rotor is further increased within this critical regime can be explained by postulating that the fraction of disturbances that is capable of causing disruption to the wake via this process increases steadily as a greater range of disturbances is able to propagate upstream against the steadily reducing velocity within the streamtube. It is not yet clear what physical process takes place to terminate such excursions and to re-establish the cylindrical topology of the wake, as is observed in the current experiment, but it is known that, within the VRS, the recirculating flow intermittently sheds away from behind the rotor disk (see, for instance, Stack *et al.* 2004), and it may be that a weakened form of this process within the critical regime might be involved in allowing the rotor to temporarily re-establish a downward flow state.

A final observation from the POD of the velocity fluctuations may yield additional insight here. Extrapolating into the third dimension, the bilateral partition of energy between the secondary POD modes at intermediate descent rates is consistent with a mechanism involving the shedding of coherent, roughly axisymmetric vortex rings into the flow below the rotor during the incipient VRS, whereas the unilateral partition of energy between the secondary POD modes at higher descent rates may be indicative of a change to a more complex asymmetric shedding mechanism within the fully developed VRS.

Although it is clear from the results of this work that a further increase in the descent rate of the rotor does indeed cause the flow to remain locked within the toroidal recirculating form associated with the fully developed VRS, it still remains an open question, in our opinions, as to whether global destabilization of the rotor wake as a result of nonlinear coupling between the loading produced on the rotor and the flow perturbations produced by these disturbances, as postulated by Leishman *et al.* (2002), Brown *et al.* (2002) and others, is fully responsible for the unique features of the flow within the fully developed VRS.

5. Conclusions

An investigation of the fluid dynamics of an experimental model of a rotor in axially descending flight has been performed using particle image velocimetry (PIV). The use of PIV has revealed the extended spatial and temporal correlations within the flow field below and around the rotor disk. At low descent rates, the flow field exhibits a cylindrical topology that is very similar to that found in hover, where the

flow is directed downwards within a streamtube extending away below the rotor. As the descent rate is increased, the hover-like flow pattern close to the rotor is increasingly encroached upon by a region of upwards flow further below the rotor. At higher descent rates, the cylindrical wake of the rotor breaks down into a toroidal recirculating flow structure in a situation known within the helicopter community as the vortex ring state (VRS). The diameter of the vortex ring is just under twice the rotor diameter, and its influence on the flow field extends for a considerable distance beyond this. At descent rates just below those where the fully developed VRS flow field is observed, the flow is highly unsteady, and analysis of the PIV results shows that in this incipient flow regime, the topology of the flow fluctuates intermittently between the down-flow topology found at lower descent rates and the flow topology found in the fully developed VRS, and the notional axisymmetry within the instantaneous flow field below the rotor is lost. Correlation analysis shows the frequency of excursions of the flow into the VRS topology to increase as the descent rate of the rotor is increased, until, within the fully developed VRS, the flow remains locked within its toroidal form. VRS defined in terms of flow topology occurs at a higher descent rate than a VRS defined in terms of thrust oscillations. These observations support a physical mechanism for the onset of the VRS in terms of the dynamics of the natural instability of the rotor wake, as suggested by recent numerical analysis, but shed new light on the detailed behaviour of the flow under incipient VRS conditions. Further experimentation to provide additional data to support theoretical postulations and to derive stability theories that are applicable to full-scale rotorcraft needs to be performed at Reynolds numbers at least an order of magnitude higher than presented in this paper. Such experimentation will clearly be challenging, as a significantly larger rotor rig would be required and the very large spatial extent of the unsteady non-axisymmetric flow field in VRS must be accounted for. This will place significant demands on the size of the testing facility and on the performance of the instrumentation.

REFERENCES

Betzina, M. 2001 Tiltrotor descent aerodynamics: a small scale experimental investigation of vortex ring state. *57th American Helicopter Society Forum, Washington, DC, USA, 9–11 May.*

Bhagwat, M. & Leishman, J. 2000 On the aerodynamic stability of helicopter rotor wakes. *56th AHS' Annual Forum, Virginia Beach, VA, USA, 2–4 May.*

Brinson, P. & Ellenrieder, T. 1998 Experimental investigation of the vortex ring condition. *24th European Rotorcraft Forum, Marseille, France,* paper TE13.

Brown, R., Leishman, J., Newman, S. & Perry, F. 2002 Blade twist effects on rotor behaviour in the vortex ring state. *28th European Rotorcraft Forum, Bristol, UK.*

Brown, R., Line, A. & Ahlin, G. 2004 Fuselage and tail-rotor interference effects on helicopter wake development in descending flight. *60th Annual Forum of the American Helicopter Society, Baltimore, MD, USA, 7–10 June.*

Drees, J. & Hendal, W. 1951 Airflow patterns in the neighbourhood of helicopter rotors. *J. Aircraft Engng* **23**, 107–111.

Glezer, A., Kadioglu, Z. & Pearlstein, A. 1989 Development of an extended proper orthogonal decomposition and its application to a time periodically forced plane mixing layer. *Phys. Fluids* A **1**, 1363–1373.

Green, R., Doolan, C. & Cannon, R. 2002 Measurements of the orthogonal blade–vortex interaction using a particle image velocimetry technique. *Exps Fluids* **29**, 369–379.

Johnson, W. 2004 Model for vortex ring state influence on rotorcraft flight dynamics. *4th American Helicopter Society Decennial Specialists' Conference on Aeromechanics, San Francisco, CA, USA, 21–23 January.*

Leishman, J. 2000 *Principles of Helicopter Aerodynamics*. Cambridge University Press.

Leishman, J., Bhagwat, M. & Ananthan, S. 2002 The vortex ring state as a spatially and temporally developing wake instability. *AHS International Specialists' Meeting on Aerodynamics, Acoustics, Test & Evaluation, San Francisco, CA, USA, 23–25 January*.

Newman, S., Brown, R., Perry, F., Ahlin, G., Simons, I., Modha, A. & Khelifa, M. 2004 Revisiting the effects of blade geometry on rotor behaviour in descending flight. *30th European Rotorcraft Forum, Marseilles, France*.

Newman, S., Brown, R., Perry, J., Lewis, S., Orchard, M. & Modha, A. 2003 Comparative numerical and experimental investigations of the vortex ring phenomenon in rotorcraft. *J. Am. Helicopter Soc*. **48**, 28–38.

Noguiera, J., Lecuona, A. & Rodriguez, P. 1997 Data validation, false vectors correction and derived magnitudes calculation on piv data. *Meas. Sci. Technol*. **8**, 1493–1501.

Spalart, P. 2003 On the simple actuator disk. *J. Fluid Mech*. **494**, 399–405.

Stack, J., Caradonna, F. & Savaş, O. 2004 Flow visualizations and extended thrust time histories of rotor vortex wakes in descent. *4th American Helicopter Society Decennial Specialists' Conference on Aeromechanics, San Francisco, CA, USA, 21–23 January*.

Stewart, W. 1951 Helicopter behaviour in vortex ring conditions. *Aeronaut. Res. Council, R&M 2735*.

Washizu, K., Azuma, A., Koo, J. & Oka, T. 1966 Experiments on a model helicopter rotor operating in the vortex ring state. *J. Aircraft* **3**, 225–230.

Widnall, S. 1972 The stability of a helical vortex filament. *J. Fluid Mech*. **54**, 641–663.

Yaggy, P. & Mort, K. 1963 Wind-tunnel tests of two vtol propellers in descent. *NASA TN* D-1766.